doi:10.20944/preprints202010.0299.v2

1 Title

Shale Compaction Kinetics

2 Authors Information

By James Edward Smith†, Phillips Petroleum, ret., and
Edward Millard Smith-Rowland‡, Alion Science and Technology
†Corresponding author; edsmith6@hotmail.com. 1209 Harris Dr, Bartlesville, OK 74006.
‡ esmithrowland@gmail.com. 3113 Edgewood Rd, Ellicott City, MD 21043-3419.

3 Abstract

The grain-to-grain stress vertically in sediments is given by the overburden less the pore fluid pressure, σ, divided by the fraction of the horizontal area which is the supporting matrix , $(1 - \varphi)$, where φ is the porosity. It is proposed that the fractional reduction of this ratio, Λ, with time is given by the product of $\varphi^{4m/3}$, $(1 - \varphi)^{4n/3}$, and one or more Arrhenius functions $A \exp(-E/RT)$ with m and n close to 1. This proposal is tested for shale sections in six wells from around the world for which porosity-depth data are available. Good agreement is obtained above 30-40 C and porosities less than 0.5. Single activation energies for each well are obtained in the range 15-33 kJ/mole, close to pressure solution of quartz, 24 kJ/mol. Values of m and n are in the range 1 to 0.8, indicating nearly fractal pore-matrix spaces and water-wet interfaces. Results are independent of over- or under-pressure of pore water. This model explains shale compaction quantitatively. Given porosity-depth data and accurate activation energy, E, one can infer paleo-geothermal-gradient and from that organic maturity, thus avoiding unnecessary drilling.

4 Keywords

Shale compaction, kinetics, activation energy, pore interfaces, grain interfaces, fractals, organic maturity

5 Introduction

For overburden S and pore pressure p, the vertical stress difference

$$\sigma \equiv (S - p), \tag{1}$$

can be changed by sedimentation, erosion or fluid flow through rock in this one-dimensional model. Similarly σ divided by the fractional area of solid matrix $(1-\varphi)$ supporting this stress can be relieved by pressure solution, breakage, relative movement of grains or fluid flow.

$$\Lambda \equiv (S - p)/(1-\varphi) = \sigma/(1-\varphi). \tag{2}$$

Differentiating with respect to time gives

$$\frac{dln\Lambda}{dt} = -\frac{dln(1-\varphi)}{dt} + \frac{dln\sigma}{dt}\ . \tag{3}$$

The first term deals with local porosity changes, while the second term deals with deposition, erosion, and fluid flow. The second term was treated previously [1] [2] [3].
Focus here is on the first term, proposing and supporting with data a chemical-type expression describing the time evolution of the vertical grain-to-grain pressure, or frame pressure.

6 Kinetic Equation and Experimental Tests

It is proposed that the reactions to reduce the frame pressure are proportional to the frame pressure Λ, to the pore surface area, $\varphi^{1.33}$, to the frame surface area, $(1-\varphi)^{1.33}$, and to one (or a sum of) Arrhenius factors, $A \exp -E/RT$. The exponent $1.33 = 4/3$ is the fractal dimension of a percolation front and twice the surface dimension $2/3$ of smooth solids. R is the ideal gas constant (8.314J/(mol degK), T is temperature in Kelvin. The fractional change in Λ thus proposed and supported is

$$\left.\frac{\partial(ln\Lambda)}{\partial t}\right|_{\sigma} = -(\varphi S_w)^{1.33m}(1-\varphi)^{1.33n}Ae^{-E/(RT)} \tag{4}$$

or equivalently

$$\left.\frac{\partial(ln(1-\phi))}{\partial t}\right|_{\sigma} = +(\varphi S_w)^{1.33m}(1-\varphi)^{1.33n}Ae^{-E/(RT)}. \tag{5}$$

The Arrhenius frequency factor, A, is not expected to depend on T for the surface reaction. Here m and n are expected to be close to 1.0 and greater than 0.5, contact areas being less than fractal because of the finite size of atoms. m and n may be different because water-to-grain and grain-to-grain interfaces differ. Notably this mechanism is primarily a dimensional argument and lacks terms relating to the sizes, shapes, and composition of pores and grains. (For different approaches see [4]).
Fractional water saturation, S_w might reduce compaction but is set to 1 and omitted hereafter.
Equation 5 indicates that if both sides are multiplied by the 'surface correction',

$$\varphi_{av}{}^{1.33m}(1-\varphi_{av})^{1.33n}/(\varphi^{1.33m}(1-\varphi)^{1.33n}), \tag{6}$$

the right hand side (RHS) will be independent of porosity,

$$\frac{\partial(ln(1-\varphi)}{\partial t}\bigg|_{\sigma}(\varphi_{av}^{1.33m}(1-\varphi_{av})^{1.33n})/(\varphi^{1.33m}(1-\varphi)^{1.33n}) = Ae^{-E/(RT)}(\varphi_{av}^{1.33m}(1-\varphi_{av})^{1.33n}). \quad (7)$$

φ_{av} is the average over the 'well' which helps visualization by minimizing movement of data on individual plots and among plots.

Equation 7 means porosity itself must be constant in the LHS as well. This can be checked by transforming the experimental porosities in 'well' porosity-depth plots, as indicated, and shown here for six examples [5] [6] [7] [8] [9]. The examples are referred to here as 'wells' although they often combine porosities from several local wells. The Macran porosity data sets are inferred entirely from seismic data, not well data. The "Sulu Sea" data are a composite of several mostly unspecified wells.

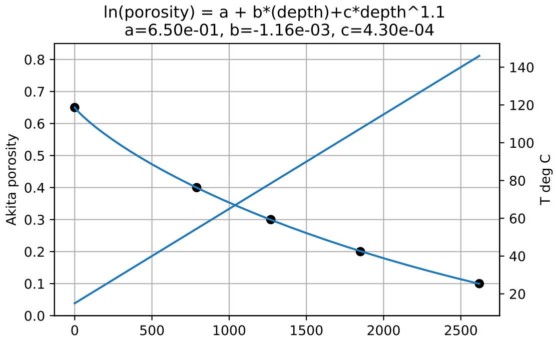
ln(porosity) = a + b*(depth)+c*depth^1.1
a=6.50e-01, b=-1.16e-03, c=4.30e-04

Figure 1 Akita well porosity data trend (Aoyagi 1980) Depth m

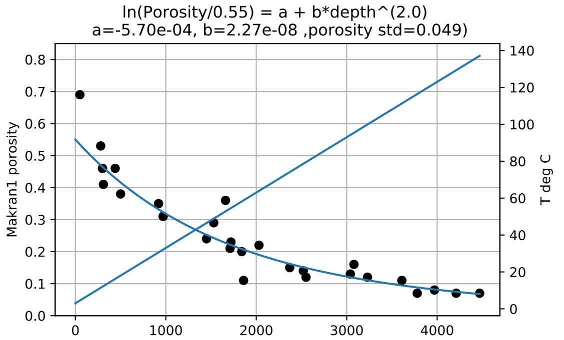
ln(Porosity/0.55) = a + b*depth^(2.0)
a=-5.70e-04, b=2.27e-08 ,porosity std=0.049)

Figure 2 Makran1 well porosity data trend (Fowler 1985) Depth m

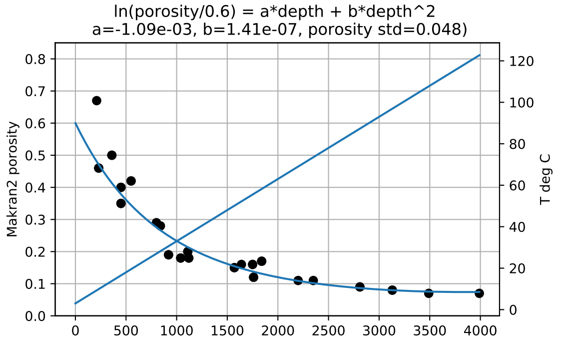
ln(porosity/0.6) = a*depth + b*depth^2
a=-1.09e-03, b=1.41e-07, porosity std=0.048)

Figure 3 Makran2 well porosity data trend (Fowler 1985) Depth m

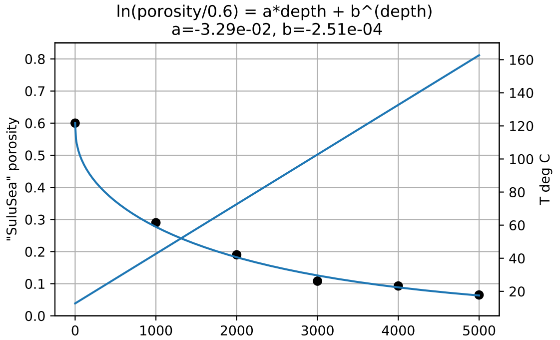
ln(porosity/0.6) = a*depth + b^(depth)
a=-3.29e-02, b=-2.51e-04

Figure 4"SuluSea" well porosity data trend (Velde 1996) Depth m

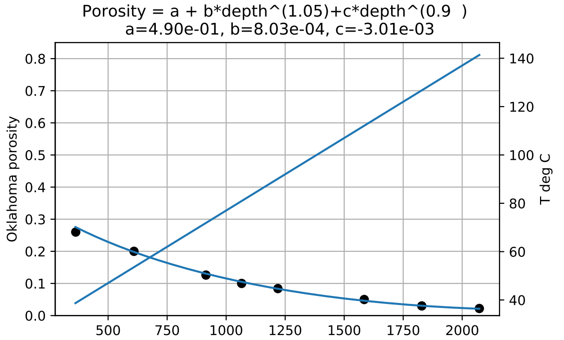
Porosity = a + b*depth^(1.05)+c*depth^(0.9)
a=4.90e-01, b=8.03e-04, c=-3.01e-03

Figure 5 Oklahoma well porosity data trend (Athy 1930) Depth m

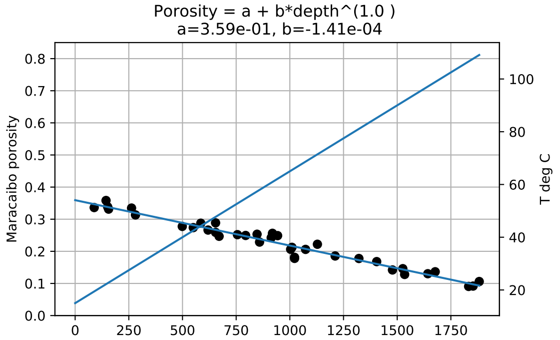
Porosity = a + b*depth^(1.0)
a=3.59e-01, b=-1.41e-04

Figure 6 Maracaibo well porosity data trend (Hedberg 1936) Depth m

Figures 1-6 show the experimental example porosity-depth relations which were discussed recently [10] [11]. Curve fit equations are shown at the top of each plot. As seen in the figures the plotted maximum paleotemperature is always assumed to be a linear function of depth, separately for each 'well'.

It is perspicuous to view transformed porosities versus Λ as a more fundamental variable than depth, common to all 'wells'. Figures 7-12 show

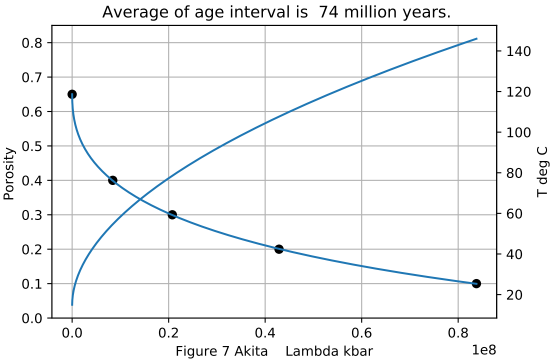

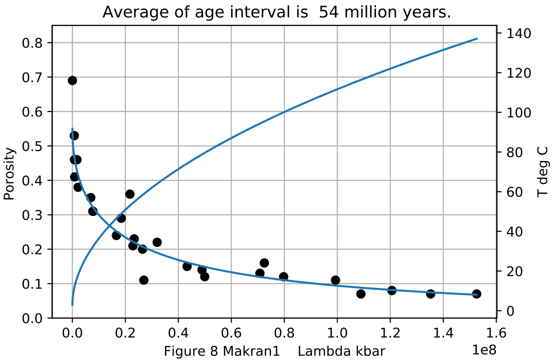

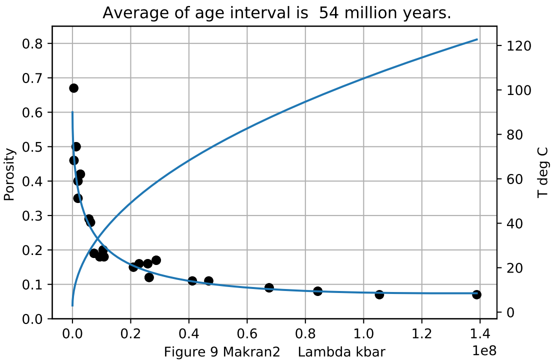

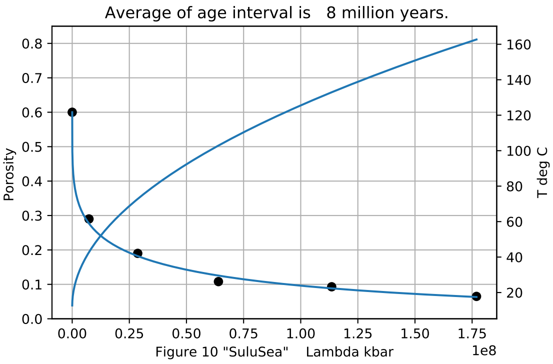

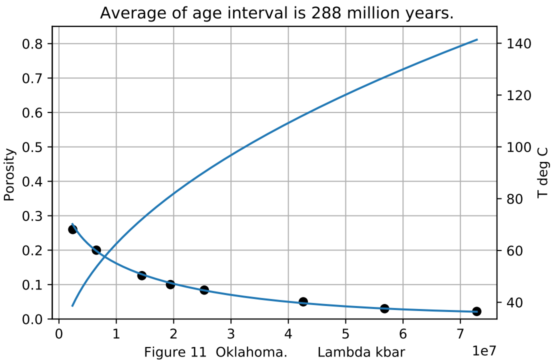

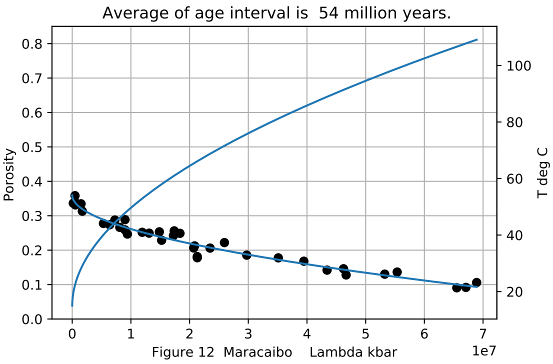

the porosity data versus an approximate Λ horizontal axis. (The approximation $p_w = g\rho_w z$ for normal water pressure is used to approximate the Λ axis as

$$\Lambda \approx g\frac{(\rho_g - \rho_w)}{(1-\varphi)}\int_0^z (1-\varphi)dz. \tag{8}$$

Here z is sample depth and depth 0 is the sediment-water or -air interface, briefly referred to as the mudline. The grain density and water density are ρ_g and ρ_w. The water pressures in these wells were not given.) Any mismatch of experimental porosity with approximate Λ is not important for illustrative purposes as porosity data points in non-normally-pressured zones are only shifted horizontally, e. g., overpresssured zones appear shifted to the right, and transformed porosity points are shown here next to be nearly constant.

Figures 13-18 show the porosities after the 'surface correction' Equation 6-7. The corrected deeper porosities have largely moved toward a common value.

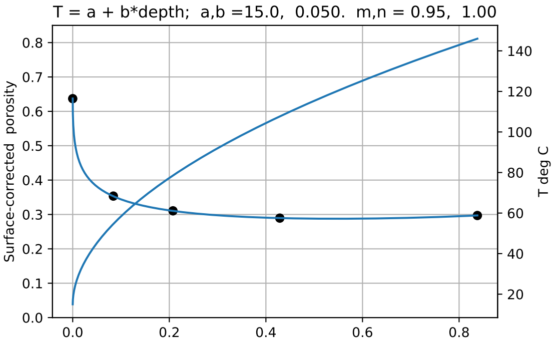

Figure 13 Akita. Lambda kbar

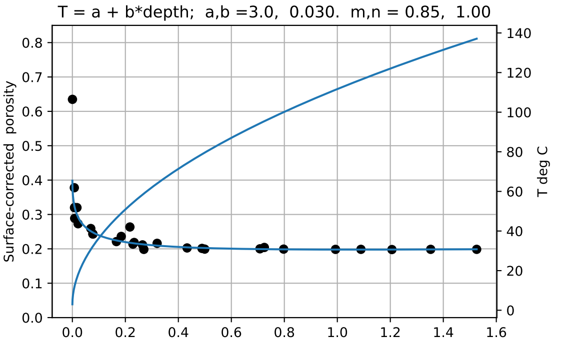

Figure 14 Makran1. Lambda kbar

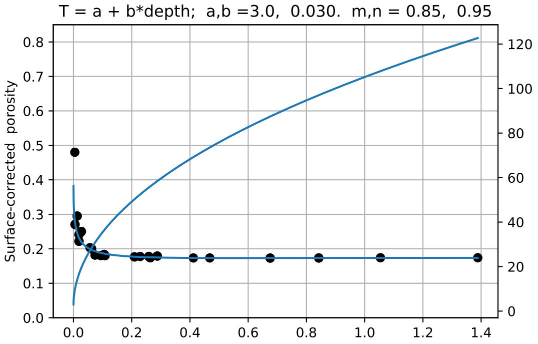

Figure 15 Makran2. Lambda kbar

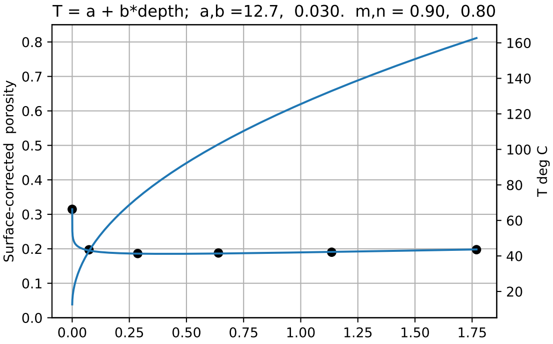

Figure 16"SuluSea". Lambda kbar

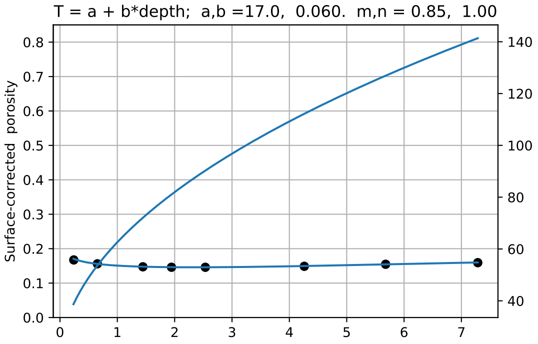

Figure 17 Oklahoma. Lambda kbar

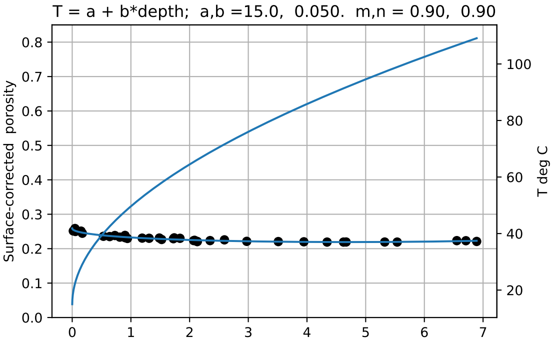

Figure 18 Maracaibo. Lambda kbar

These figures indicate that the reaction is slow at temperatures below 30-40 C., and that longer geologic times (Table 1) produce greater compaction effects.

At porosities greater than 0.5 Equation 4 can have multiple porosity values give the same number, as it has the logistic form. This agrees with deep sea studies which show porosities are chaotic [6] at porosities greater then 0.5. Porosities greater than 0.5 are excluded here in estimating activation energies.

7 Results

Equation 4 is supported in that, after the 'correction', porosities in each well have approached a common value except for shallow chaotic low-temperature portions. Table 1 gives the ratio of the scatter (entropy) of the porosities after the correction to the entropy before the corrections. The convergence of the transformed porosities is good above 30-40 C and at porosities below 0.5.

An estimate of activation energy, E, can be made by plotting the logarithm of the left hand side of Equation 9 versus $-1/RT$. The common φ_{av} terms in Equation 7 are cancelled here

$$\varphi^{-1.33m}(1-\varphi)^{-1.33n}\left.\frac{\partial(ln(1-\varphi))}{\partial t}\right|_{\sigma} = Ae^{-E/RT}. \tag{9}$$

The partial derivative requires an approximation. Breaking geologic time τ into many, N, small time increments δt it is seen that each term in the sum below is the instantaneous time derivative $ln((1-\varphi_i)/(1-\varphi_{i-1}/\delta t$ for that time. The sum is the average over time of these instantaneous time derivatives and, like the pages of a book, add up to give the (large) finite-difference approximation on the right below, equivalent to only the starting and ending pages of the book as it were.

$$\Sigma_1^N ln\frac{(1-\varphi_i)}{(1-\varphi_{i-1})}\Big/ N\delta t = ln\frac{(1-\varphi)}{(1-\varphi_0)}\Big/|\tau| \tag{10}$$

Here we have put $\varphi_N = \varphi$, the current porosity. φ_0 would be the seabed porosity to prevent negative values of the logarithm, but is 0.5 to analyze deeper shales and avoid chaotic behavior close to the seabed.

Porosity changes due to lateral forces and vertical forces are obviously included in the summation of the average, Equation 12, which is used in place of the partial derivative,

$$\frac{\partial(ln(1-\varphi)}{\partial t}\bigg|_\sigma \to ln\frac{(1-\varphi)}{(1-\varphi_0)}\Big/|\tau|. \tag{11}$$

This partial derivative on the left of Equation 11 would have come up in the same way if σ, Equation 3, represented horizontal forces rather than vertical forces. This approximation, or replacement, thus represents overall porosity reduction due to the combined forces and temperatures acting, in natural order, and including changes in overburden and pore fluid pressure, to reduce the potential energy Λ. This replacement is more appropriate than the partial derivative for computing activation energy, and further cannot be avoided since the actual porosity data result from all these factors. Putting this approximation into Equation 9 gives

$$\varphi^{-1.33m}(1-\varphi)^{-1.33n} ln\frac{(1-\varphi)}{(1-\varphi_0)}\Big/\tau = Ae^{-E/RT} \tag{12}$$

Multiplying the LHS with a constant K to compensate for a possible mis-estimate would not change the estimate of E, as taking the slope of the logarithm of Equation 12 drops out K. Assuming deposition occurs over a time short compared the geologic age range, Table 1, with no important unconformities, τ is approximately constant also. Thus

$$E = -\Delta(ln(LHS^*)/\Delta(1/RT^*), \tag{13}$$

where the * superscript means at temperatures above $\approx$ 40C and porosities less than 0.5. (A 60C cut-off produces similar results.) With this E a rough approximate A is obtained, Table 1,

$$A = (LHS^*)\exp(E/RT^*). \tag{14}$$

This A estimate would contain poorly known τ and any K. K = 1 is used. The average of the top and bottom geologic time boundaries for a 'well' is taken for τ in computing A. Plotting the log of the LHS versus $-1/RT$ gives E for the six 'wells', Figures 19-24.

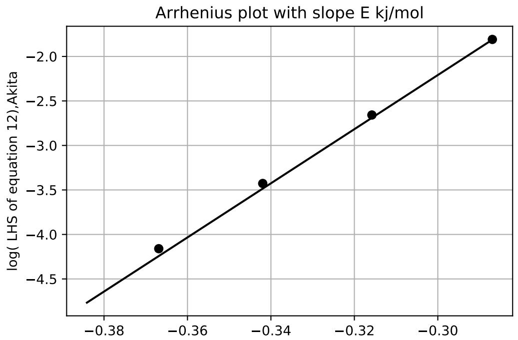

Figure 19-1/RT. Akita, Aoyagi etal. 1980 1/kJ mol

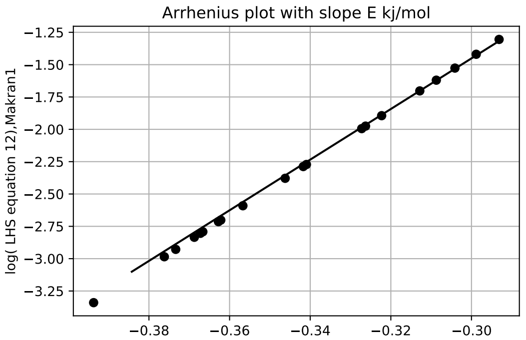

Figure 20 -1/RT. Makran1, Fowler etal 1985 1/kJ mol

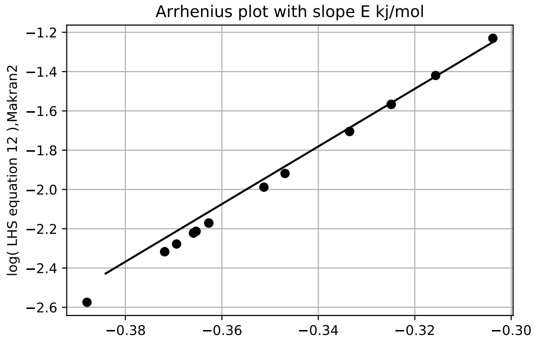

Figure 21 -1/RT. Makran2, Fowler etal 1985 1/kJ mol

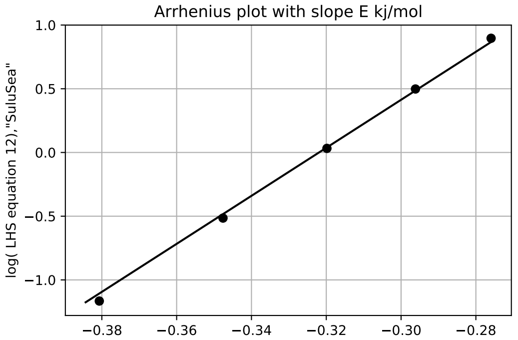

Figure 22 -1/RT. "SuluSea", Velde 1996 1/kJ mol

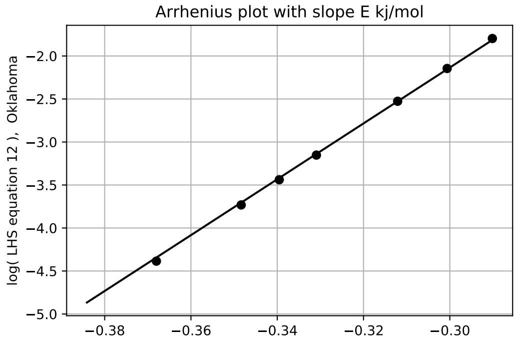

Figure 23 -1/RT. Oklahoma, Athy 1930 1/kJ mol

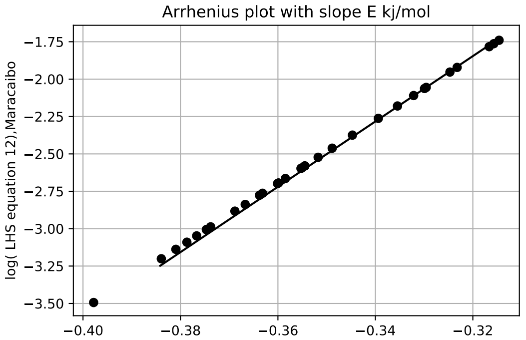

Figure 24 -1/RT. Maracaibo, Hedberg 1936 1/kJ mol

As shown in Table 1 the E's vary from 15 to 33 kJ/mol, averaging 23+-6 kJ/mol. Laboratory measurements of the pressure solution of quartz aggregates [12] give 24 kJ/mol, suggesting that this is the rate-limiting reaction occurring in shales.

8 Discussion and Data

Map coordinates were known only for the Makran 'wells'. Temperatures were not available for any wells. Paleo mudline temperature estimates are made on the basis of paleoenvironments [5], paleolatitude, and geologic age, Table 2. Mudline temperatures of 3 C are assigned to wells from abyssal plains. Shallow sea or lake environments are assigned expected land paleotemperatures, corrected for paleolatitudes, and for any intervening high temperature events such as the Eocene high [13]. If two estimates are made they are averaged. The mudline temperature used for the Sulu Sea, 13 C, was known for the deepest point [14].

These paleo-mudline-temperature estimates are less important to this study than are paleo-geothermal-gradients, as the compaction reaction found here becomes noticable deeper at the higher 'well' temperatures and porosities less than 0.5. Because the Earth is cooling as radioactivity and initial energy of assembly decline, and because these wells were drilled/investigated in areas where temperatures were supposed to be high enough to generate petroleum, minimum paleo-geothermal-gradients of .03 C/m were initially assigned. The 'well' mudline and temperature gradient estimates used here are well within present day experience [15].

A paleo-geothermal-gradient of .05 C/m was assigned to the Akita 'well', and to Maracaibo back-arc well, on the basis of necessary thermal maturity [5].

In Northeast Oklahoma nearby sedimentary rock mineralization and granite outcrop suggest a higher paleo-geothermal-gradient, perhaps .06 C/m as assigned, Table 1. Averaging the E's computed from all these provisional temperature gradient assignments, along with the one laboratory measurement, gives an average activation energy of 23+-6 kJ/mol. With this E_{av} an Oklanoma paleo-geothermal-gradient of 0.12 C/m was inferred. Using this average assumes the same mechanism occurs in all wells. With this E_{av}, paleo-geothermal-gradients for the other wells were also obtained. These 'improved' estimates with other recalculated parameters are shown in Table 3 as far as data convergence allowed. Differences in porosity determination method might have impacted activation energy determinations, e.g., Oklahoma and Maracaibo porosities were measured on hand samples, while as mentioned the Macron porosities are inferred from seismic data.

Current temperature profiles are known privately for thousands of wells. This information would help gain an accurate E_{av}, especially for deep-water wells where the paleo-mudline temperature is probably ~ 3 C. Laboratory data for pressure solution of quartz and other minerals can be expanded to higher temperatures and pressures to check current ideas.

The Makran data, Figures 2 and 3, show that lateral forces in the accretionary wedge (Makron2) produced porosities reduced from nearby abyssal plain (Makron1) porosities. There the major lithology need not be clay throughout, as good reflectors were needed to produce data. The low Oklahoma porosities were also thought to have been reduced by lateral forces [8] [9]. Directionally variant lateral forces are often observed in horizontal drilling [16]. The compaction response mechanism to both vertical and horizontal forces is probably the same, Equation 4.

9 Conclusions

Equation 4 explains shale compaction at temperatures above ≈ 35 C with activation energies E $\approx$ 23+-6 kJ/mol, close to 24 kJ/mol for the pressure solution of quartz. Problems of mineralogy, grain shapes and sizes, permeability, overpressures and pore connectivity are by-passed. The results support nearly fractal pore interfaces with m and n between .8 and 1. The reduction in Λ is also modeled as proportional to geologic age to the first power. By Equation 12 the one-dimensional problem is recognized as three spatial dimensions. In obtaining activation energy the geologic age approximately drops out if there are no unconformities. The problem of chaotic porosity data at porosities greater than 0.5 is recognized and avioded. Provisional paleotemperature gradients are used to obtain activation energies which are averaged to bootstrap to hopefully better paleotemperature gradients. Given porosity data from the known or, in cases of later erosion, an estimated pre-erosional depth, along with an average activation energy, E_{av}, one can infer or rank maximum paleo-geothermal-gradients and from that organic maturity, thus avoiding unnecessary drilling.

10 Tables

Table 1: Derived variables for initially assumed paleotemperatures

Basin Location	Basin type	Age range my	E kJ/mol	A 10^{15}/sec	Entropy, relative	m	n
Akita, Hokkaido	back-arc	1.5-146	30	67	0.9	.95	1.0
Makran1	abyssal	2.6-105	20	7	0.7	.85	1.0
Makran2	abyssal	2.6-105	15	2	0.7	.85	.95
Sulu Sea	deep-water	0-15	19	27	0.6	.90	.80
Oklahoma	convergent	254-323	33	97	0.2	.85	1.0
Maracaibo	back-arc	2.6-105	21	7.8	0.5	.90	.90

Table 2: Description and initial parameters for wells

Basin Location	Basin type	Age range my	Paleo-mudline C	Paleo ∇T C/m	References
Akita, Hokkaido	back-arc	1.5-146	(3+13+13)/2	.05	Aoyagi et al. pp 41
Makran1	abyssal	2.6-105	3	.03	Fowler et al.
Makran2	abyssal	2.6-105	3	.03	pp 429-430
Sulu Sea	deep-water	0-15	13	.03	Velde pp 196
Oklahoma	convergent	254-323	(7+14+13)/2	.06	Athy pp 12
Maracaibo	back-arc	2.6-105	(3+14+13)/2	.05	Hedberg pp 254

Table 3: Inferred parameters for E_{av} = 23+-7 kJ/mol

Basin Location	Age range my	Paleo ∇T C/m	E kJ/mol	A 10^{16}/sec	Entropy, relative	m	n
Akita, Hokkaido	1.5-146	0.06	28	1	.3	.95	1.0
Makran1	2.6-105	0.019	22	6	.6	.85	1.0
Makran2	2.6-105	0.017	19	3	.6	.85	.95
Sulu Sea	0-15	0.022	23	16	.4	.90	.80
Oklahoma	254-323	0.12	23	0.1	.5	.85	1.0
Maracaibo	2.6-105	0.046	23	2	.5	.90	.90

11 Acknowledgments

Gary M. Hoover clarified obscurities and limitations in the progression of this paper.

12 Author contributions

All work was carried out by corresponding author James Edward Smith 85, with physicist son Edward Millard Smith-Rowland as backup due to age and Covid 19 threat.

13 Funding

This research received no external funding.

14 Conflicts of interest

The authors declare no conflict of interest.

15 References

References

[1] Smith, J. E. The dynamics of shale compaction and evolution of pore-fluid pressures. *J Inter Assoc for Mathematical Geology* **1971** ,*3 3*, 239 - 263.

[2] Smith J. E. Shale compaction. *Trans SPE of AIME* **1973** ,*255*, 12 - 22.

[3] Smith J.E., Dysinger G.C., Borst R.L. Shales and abnormal pressures. In *Geotechnical and Environmental Aspects of Geopressure Energy* ; Saxena, S. K., Ed.; Engineering Foundation: New York, USA, 1980; pp. 69-91, ISBN 0-939204-03-7

[4] Yang X., Pressure solution in sedimentary basins: effect of temperature gradient. *Earth and Planetary Sci Letters* **2000** ,*176 2*, 233 - 243.

[5] Aoyagi K., Asakawa T. Primary migration theory of petroleum and its application to petroleum exploration. *Organic Geochem* **1980** ,*2*, 33 - 43.

[6] Fowler S.R., White R.S., Louden K.E. Sediment dewatering in the Makran accretionary prism. *Earth and Planetary Science Letters* **1985** , *75 4* , 427 - 438.

[7] Velde B. Compaction trends of clay-rich deep sea sediments. *Marine Geology* **1996** , *133 3-4* , 193 - 201.

[8] Athy L.F. Density, porosity, and compaction of sedimentary rocks. *Amer Assoc of Petroleum Geol Bull* **1930** , *14 1* , 1 - 24.

[9] Hedberg H.D. Gravitational compaction of clays and shales. *Amer J of Science* **1936** ,*31 184* , 241 - 287.

[10] Mondol N.H. ,Bjrlykke K, Jahren J, Heg K Experimental mechanical compaction of clay mineral aggregates. Changes in physical properties of mudstones during burial. *Marine and Petroleum Geol* **2007** ,*24 5*, 289 - 311.

[11] Puttiwongrak A., Giao P.H., Vann S. An easily used mathematical model of porosity change with depth and geologic time in deep shale compaction. *Inter J of GEOMATE* **2020** , *19 73* , 108-115.

[12] Miyakawa K., Kawabe I. Pressure solution of quartz aggregates under low effective stress (0.420.61 MPa) at 2545 C. *Applied Geochem* **2014** , *40*, 61 - 69.

[13] Janke P.R. (2013) A correlated history of Earth. *The worldwide museum of natural history.* ,*Pan Terra Inc.* **2013** 1.

[14] Lukens R.R. Surveying the Phillipine Islands. *NOAA History; Merchant Marine Bull* **1931** , *Apr* , 10,11,32.

[15] Christie C.H., Nagihara, S. Geothermal gradients of the northern continental shelf of the Gulf of Mexico. *Geosphere* **2016** ,*12 1*, 26 - 34.

[16] Bjornen, K *Private communication* **2019**

999